ChemComm

COMMUNICATION

View Article Online
View Journal | View Issue

Cite this: *Chem. Commun.*, 2024, **60**, 5968

Received 21st February 2024,
Accepted 4th May 2024

DOI: 10.1039/d4cc00850b

rsc.li/chemcomm

Zn^{2+}-storage mechanism in V_6O_{13} with nanosheets for high-capacity and long-life aqueous zinc-metal batteries†

Lineng Chen,‡[a] Wenwei Zhang,‡[a] Jianyong Zhang[a] and Qinyou An *[ab]

V_6O_{13} with a nanosheet structure was employed as a cathode material for aqueous zinc metal batteries. V_6O_{13} delivered a high specific capacity of 425 mA h g^{-1}, outstanding rate performance and durable cycling with high capacity retention of 86% after 3000 cycles. Moreover, *in situ* X-ray diffractometer (XRD), *ex situ* X-ray photoelectron spectroscopy (XPS) and X-ray absorption near-edge structure (XANES) were employed to ascertain the reaction mechanism of Zn^{2+} storage.

Recently, the aqueous zinc metal battery (AZMB) has received considerable attention because it has a water-based electrolyte with high safety and fast conductivity of ions.[1–3] Also, low-cost metal zinc as the anode can cycle stably in the aqueous electrolyte directly, but also has high specific capacity and a suitable redox potential. However, further development of the AZMB is required, especially finding suitable cathode materials with considerable capacity and a stable structure for the reversible insertion/extraction of zinc ions with high charge density.[4,5]

Some developed cathodes, including typical Mn-, V-, PBAs- and organic-based materials, have demonstrated acceptable storage of Zn^{2+}.[1,6–8] In general, Mn-based materials deliver poor cycling performance caused by Mn-element dissolution due to the Jahn–Teller effect. PBAs with unutilized active sites usually exhibit lower specific capacity than other cathode materials. Moreover, the organic cathode will have dissolution issues and produce side-products to damage the zinc anode. Compared with the cathode materials stated above, vanadium-based materials have received increasing attention. This is because of their multiple valence states (+3, +4 and +5) for higher capacity than other types of materials and a suitable structure to achieve favourable Zn^{2+} insertion/extraction.[9,10] Thus, vanadium oxides and their corresponding analogues may be promising cathode materials for AZMB.[11–13]

Among vanadium-based materials, low-cost V_6O_{13} usually exhibits high specific capacity, excellent thermal stability and wide availability in metal-ion batteries, particularly alkali ion-based batteries with an organic electrolyte.[14] V_6O_{13} has a monoclinic crystal system. It consists of a single octahedron and a deformed bi-octahedron, which are connected together in common vertices. Then, it extends indefinitely along the direction shape [010] in the form of common edges to form a tunnel, which can ensure reversible-charge ions insert/extract into/from host materials. V_6O_{13} of mixed valence (V^{5+}/V^{4+}) also delivers high electronic conductivity to ensure ultrafast charge/electron transfer.[15–17]

However, the crystal lattice will expand if zinc ions are constantly removed in V_6O_{13}, which may make the crystal structure unstable due to the metastable structure of V_6O_{13} and lead to poor cycling performance. In this case, the free-binder,[17] ion preinsertion[18] and defect strategy[19] as well as heterostructured V_6O_{13}[20,21] have been developed as the cathode for an AZMB. Although it has achieved better performance than a cathode made of pure V_6O_{13}, the potential issues and challenges merit extra attention in subsequent research. Typically, the free-binder cathode usually grows V_6O_{13} on the inactive carbon cloth or other metallic substrates with weight, which can reduce the energy density. Moreover, alien species will occupy the storage sites and produce electrostatic repulsion with Zn^{2+}. Also, the oxygen defect may cause a structural decline due to some missing supporting atoms. In addition, the heterostructured V_6O_{13} usually has a complex mechanism for Zn^{2+} storage and should be analysed further with the help of advanced characterization methods. Notably, the development of cathode materials with a special morphology and structure can increase the permeability of the electrolyte to reduce the diffusion path of Zn^{2+}, but also alleviate the stress changes caused by repeated insertion/extraction of Zn^{2+}. Thus, the structural stability of the cathode material is enhanced for a considerable performance and the effect of lattice expansion is

[a] *State Key Laboratory of Advanced Technology for Materials Synthesis and Processing, Wuhan University of Technology, Wuhan 430070, China. E-mail: anqinyou86@whut.edu.cn*
[b] *Hubei Longzhong Laboratory, Wuhan University of Technology (Xiangyang Demonstration Zone), Xiangyang, 441000, P. R. China*

† Electronic supplementary information (ESI) available: Experimental section and supplementary figures. See DOI: https://doi.org/10.1039/d4cc00850b

‡ Lineng Chen and Wenwei Zhang contributed equally to this work.

reduced thanks to the special micro/nano structure. Moreover, understanding the zinc-storage mechanism of V_6O_{13} *via* advanced characterization methods is lacking, but it is crucial for the subsequent modification of cathode materials.

Herein, V_6O_{13} with ultrathin nanosheets was prepared as the cathode for an AZMB *via* simple hydrothermal and subsequent heat-treatment methods. Information on the morphology, structure and chemical bonds was obtained *via* SEM and Raman spectroscopy. The Zn^{2+}-storage ability was evaluated in a mildly acidic electrolyte of 1 M $Zn(CF_3SO_3)_2$. Importantly, the Zn^{2+}-storage mechanism was demonstrated through the *in situ* X-ray diffraction (XRD), *ex situ* X-ray absorption near-edge structure (XANES) and X-ray photoelectron spectroscopy (XPS). This work may provide promising cathode materials for the further development of AZMBs and other metal-ion batteries.

V_6O_{13} nanosheets could be prepared by hydrothermal synthesis and subsequent heat treatment. First, $NH_4V_4O_{10}$ micro-flowers with an ultrathin petal-like structure and poor crystallinity were synthesized by a simple hydrothermal method (Fig. 1a and Fig. S1, S2, ESI†). After washing and drying, ultrathin V_6O_{13} nanosheets were obtained by calcination at 450 °C for 8 h under a nitrogen atmosphere according to eqn (1). In this process, NH_3 decomposed from $NH_4V_4O_{10}$ acts as a reducing agent to facilitate the production of mixed-valence vanadium with high electrical conductivity. Moreover, the nanosheets could shorten the diffusion path of Zn^{2+} and increase the contact area of host materials and electrolyte to promote the transfer kinetics of Zn^{2+}.

$$18\ NH_4V_4O_{10} \rightarrow 12\ V_6O_{13} + 24\ H_2O + 5\ N_2 + 8\ NH_3 \qquad (1)$$

Accordingly, SEM demonstrated that the morphology of the precursor changed from micro-flowers to random flakes of V_6O_{13} during heat treatment. V and O elements were evenly distributed in SEM mapping images (Fig. 1c and Fig. S3, S4, ESI†).

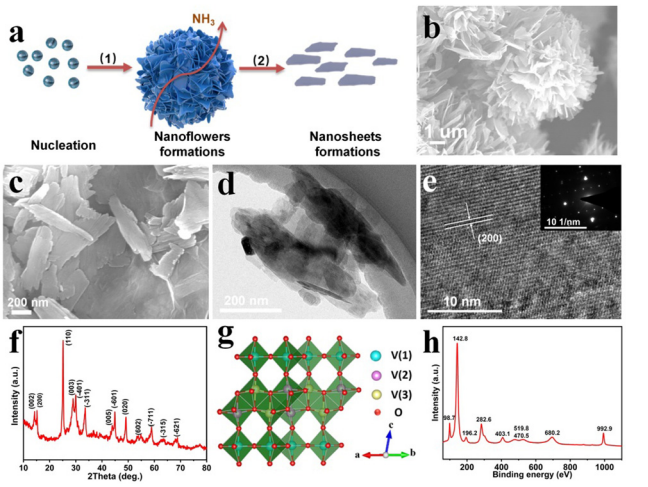

Fig. 1 (a) Preparation of V_6O_{13}. (b) SEM of precursor $NH_4V_4O_{10}$. (c) SEM of prepared V_6O_{13}. (d) TEM image. (e) HRTEM image and SAED pattern of V_6O_{13}. (f) and (g) XRD pattern and corresponding crystal-structure model of V_6O_{13}. (h) Raman spectra.

Meanwhile, this sheet structure was also revealed under the application of TEM. The HRTEM image showed a clear lattice spacing corresponding to the (200) plane of V_6O_{13} (Fig. 1d and e).

A different XRD pattern from the precursor showed that a new substance had been produced during calcination, and it matched well with V_6O_{13} reported in the literature.[22,23] Hence, the V_6O_{13} cathode material has been synthesized (Fig. 1f). Moreover, the crystal structure of V_6O_{13} contained three non-equivalent (but symmetric) vanadium atoms (V1, V2, and V3), and each vanadium atom was surrounded by a shared oxygen atom in a distorted VO_6 octahedron (Fig. 1g). These octahedrons formed single- and double-layer VO_X by sharing angles and edges. This unique layer structure and orientation-specific cavity could make V_6O_{13} a promising cathode material for energy-storage systems.

Peaks located at 98.7, 142.8, 196.2, 282.6, 403.1, 470.5, 519.8, 680.2 and 992.9 cm^{-1} were consistent with the reported vibrations of V_6O_{13} (Fig. 1h).[24] In general, the three Raman peaks at the low frequencies of 98.7, 142.8 and 196.2 cm^{-1} corresponded to the lattice vibration of [VO5]–[VO5], which is related to the layered structure in the material. The Raman peak at 282.6 and 403.1 cm^{-1} corresponds to the bending vibration of the V═O bond, and the Raman peak at 470.5 wave number corresponds to the bending vibration of the V–O–V bond. In addition, the Raman peaks at 519.8 and 680.2 cm^{-1} corresponded to the symmetric tensile vibrations of the V–O_3 bond and V–O_2 bond, respectively. Finally, the Raman peak at 992.9 cm^{-1} also corresponded to the symmetric tensile vibration of the V═O bond.

Thus, V_6O_{13} with a nanosheet structure had been obtained and demonstrated after characterization and corresponding analyses of results.

Subsequently, the Zn^{2+}-storage ability of V_6O_{13} was evaluated in 1 M $Zn(CF_3SO_3)_2$ electrolyte using CR-2016-type cells. First, cyclic voltammetry (CV) curves were tested within the voltage range 0.2–1.6 V, and the similar redox peaks indicated good reversibility (Fig. 2a). Fig. 2b shows the galvanostatic charge–discharge (GCD) curves in the initial five cycles. The specific discharge capacity could reach 425 mA h g^{-1} at 50 mA g^{-1}. Specifically, the cycling performance was evaluated at 0.5 A g^{-1}, and it can reach a specific capacity of 290 mA h g^{-1} and remain at 290 mA h g^{-1} after 100 cycles (Fig. 2c). Moreover, the excellent performance was demonstrated further at current densities of 0.1, 0.2, 0.5, 1.0, and 2.0 A g^{-1}, and the specific capacity almost reached the initial capacity at the first test (Fig. 2d and e). Notably, the Zn^{2+}-storage ability was demonstrated further at a high current density of 8.0 A g^{-1} and remained at 3000 stable Zn^{2+} insertion/extraction processes with an approximately capacity retention rate of 86% relative to the maximum specific capacity. The increased capacity in the initial cycling process could be attributed to activation of the material (Fig. 2f).

In general, the electrochemical properties of V_6O_{13} as a cathode material for an AZMB were better than those of some reported V_6O_{13} (Table S1, ESI†) and the precursor $NH_4V_4O_{10}$

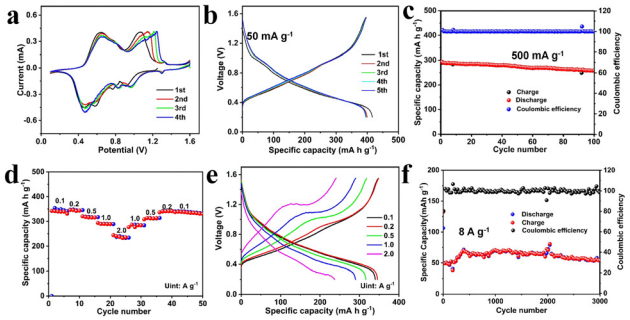

Fig. 2 (a) CV profiles. (b) GCD curves in the initial five cycles. (c) Cycling performance at 0.5 A g^{-1}. (d) and (e) Rate performance at different current densities and corresponding GCD curves. (f) Long cycling performance at 8.0 A g^{-1}.

(Fig. S5–S7, ESI†). This finding could be attributed to the rapid diffusion path provided by the nanosheet structure and electron transport facilitated by the mixed valence state of vanadium. The value of Zn^{2+} diffusion coefficients was calculated to be approximately 10^{-10} to 10^{-11} cm^2 s^{-1} (Fig. S8, ESI†), which confirmed the analysis stated above.

To further understand the energy-storage mechanism of V_6O_{13} cathodes during charging and discharging, *in situ* XRD analysis was used to characterize the structural evolution of electrode materials. The characteristic peaks of the (110) and (−311) planes shifted toward a lower theta value caused by Zn^{2+} insertion and almost back to the original state during subsequent Zn^{2+} extraction according to XRD analysis (Fig. 3a). In Fig. S9 (ESI†), the peak of the electrode in the initial state was the synthesized V_6O_{13}. At the first discharge, a series of new diffraction peaks appeared at 23.62°, 28.48°, and 34.86°, and these new peaks can be directed to the phase of $Zn_3V_2O_7(OH)_2\cdot 2H_2O$ (ZVO; JCPDS number: 50-0570).[25–27] Part of V_6O_{13} underwent irreversible phase transition in the first cycle. The V–O–V column supports the zinc-oxide layer, forming a layered ZVO with a porous structure, which facilitates the rapid migration of

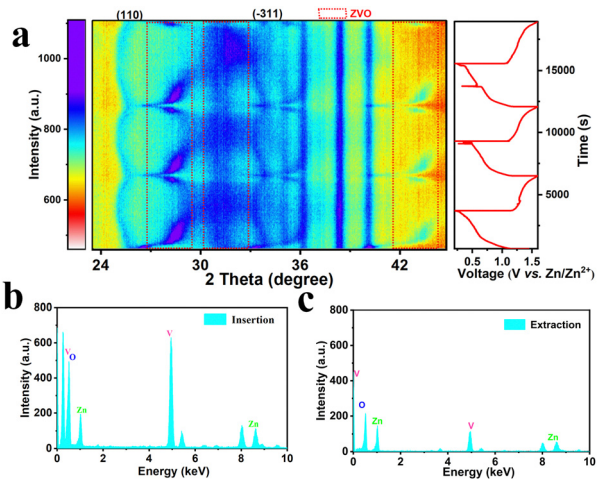

Fig. 3 (a) *In situ* XRD pattern at initial three cycles. (b) and (c) TEM-EDS at full discharge and full charge.

Zn^{2+}.[27,28] Moreover, the peak intensity weakened gradually during discharge and recovered to its original strength in subsequent cycles, which suggested good reversibility (Fig. S10, ESI†). During discharge progression, part of the peak shifted to a higher angle caused by the strong electrostatic interaction between Zn^{2+} and the vanadium oxygen layer. Electrostatic repulsion was shielded effectively, causing the crystal structure to shrink. This finding was consistent with reports of V_6O_{13}/VO_2[21] samples and the $Na_2V_6O_{16}\cdot 1.63H_2O$[29] cathode in AZMBs. Also, this reversible Zn^{2+} insertion/extraction could be demonstrated by TEM-EDS data with an obvious intensity of Zn element (Fig. 3b and c). Thus, the reversible Zn^{2+} insertion/extraction into/from V_6O_{13} had been initially demonstrated.

As shown in Fig. 4a and Fig. S11 (ESI†), there were no XPS spectra of Zn 2p at the fresh electrode, but a strong Zn signal at the fully discharged state demonstrated that Zn^{2+} could be inserted into V_6O_{13}. The significantly weakened Zn signal at the fully charged state indicated that most zinc ions could be smoothly removed, and the residual Zn^{2+} in the ZVO phase may serve as a 'pillar' to stabilize the structure for reversible Zn^{2+} insertion/extraction. Moreover, according to the XPS spectrum of V 2p (Fig. 4b–d), in the pristine V_6O_{13} electrode, the valence of main V^{5+} and part V^{4+} was mixed. Differently, the proportion of V^{5+} decreased while the proportion of V^{4+} increased significantly and V^{3+} appeared, which could maintain charge neutrality after the insertion of zinc ions. This action resulted in a decrease in the valence of vanadium at fully discharged states. Notably, there were only V^{5+} and V^{4+} signals at fully charged states, which demonstrated the reversible Zn^{2+} insertion/extraction process. Also, this *ex situ* XPS result was consistent with the other mechanistic characterization stated above.

Furthermore, the *ex situ* XANES of V_6O_{13} was characterized to obtain in-depth understanding on local electronic structures during Zn^{2+} insertion (Fig. 4e and f). Compared with the original state, the V K-edge moved slightly towards the lower binding energy at the insertion state, which indicated that the average valence state of vanadium decreased due to coordination between the zinc ion and lattice oxygen.[30] In addition, the

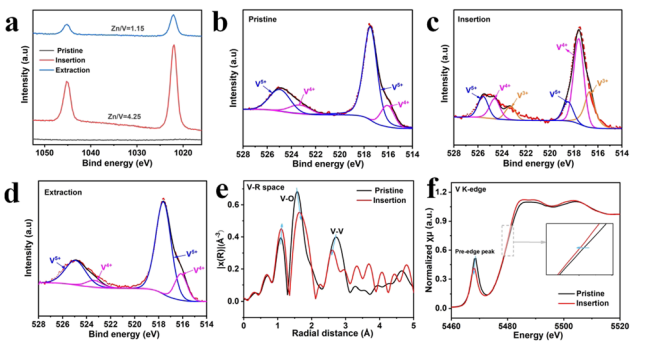

Fig. 4 (a)–(d) *Ex situ* XPS spectrum of Zn 2p and V 2p at pristine, fully inserted and extracted states. (e) and (f) *Ex situ* V K-edge XANES and V K-edge EXAFS of V_6O_{13} at different states.

variation in the pre-edge peak located at 5468.7 eV was positively correlated with the deviation from the octahedral symmetry of the vanadium site. After the insertion of zinc, the peak shifted to a lower energy position, and the intensity of the peak decreased. The corresponding Fourier transform extended X-ray absorption fine structure (FT-EXAFS) spectra (Fig. 4f) showed that after the insertion of Zn^{2+}, the length of the V–O bond increased (from 1.56 Å to 1.71 Å) and the length of the V–V bond shortened slightly (from 2.73 Å to 2.61 Å). The V–O bond is the framework of the crystal structure of V_6O_{13} materials. Hence, the small changes of chemical bonds indicated that the structure of the V_6O_{13} material had good stability during charge and discharge.

V_6O_{13} obtained by hydrothermal synthesis and subsequent heat treatment was selected as the cathode for an AZMB. V_6O_{13} delivered considerable specific capacity of 425 mA h g^{-1} and long cycling performance, such as a high capacity retention rate of 86% after 3000 cycles at 8 A g^{-1}. The reaction mechanism was revealed under application of *in situ* XRD, *ex situ* XPS and XANES. We demonstrated that V_6O_{13} could be considered a promising cathode material for AZMBs, and may provide potential electrode material for other metal-ion batteries.

This work was supported by the Natural Science Foundation of Hubei Province (2022CFA087), the National Natural Science Foundation of China (52172231).

Conflicts of interest

There are no conflicts of interest to declare.

Notes and references

1 L. E. Blanc, D. Kundu and L. F. Nazar, *Joule*, 2020, **4**, 771–799.
2 P. Ruan, S. Liang, B. Lu, H. J. Fan and J. Zhou, *Angew. Chem., Int. Ed.*, 2022, **61**, e202200598.
3 Y. Liang, H. Dong, D. Aurbach and Y. Yao, *Nat. Energy*, 2020, **5**, 646–656.
4 X. Jia, C. Liu, Z. G. Neale, J. Yang and G. Cao, *Chem. Rev.*, 2020, **120**, 7795–7866.
5 Y. Ding, L. Zhang, X. Wang, L. Han, W. Zhang and C. Guo, *Chin. Chem. Lett.*, 2023, **34**, 107399.
6 Y. Xu, G. Zhang, J. Liu, J. Zhang, X. Wang, X. Pu, J. Wang, C. Yan, Y. Cao, H. Yang, W. Li and X. Li, *Energy Environ. Mater.*, 2023, **6**, e12575.
7 S. Liu, L. Kang, J. M. Kim, Y. T. Chun, J. Zhang and S. C. Jun, *Adv. Energy Mater.*, 2020, **10**, 2000477.
8 V. Mathew, B. Sambandam, S. Kim, S. Kim, S. Park, S. Lee, M. H. Alfaruqi, V. Soundharrajan, S. Islam, D. Y. Putro, J.-Y. Hwang, Y.-K. Sun and J. Kim, *ACS Energy Lett.*, 2020, **5**, 2376–2400.
9 W. Zhang, C. Zuo, C. Tang, W. Tang, B. Lan, X. Fu, S. Dong and P. Luo, *Energy Technol.*, 2020, **9**, 2000789.
10 W. Jiang, K. Zhu and W. Yang, *Chemistry*, 2023, **29**, e202301769.
11 D. Chen, B. Wang, X. Cui, H. Yang, M. Lu, D. Cai and W. Han, *Chem. Commun.*, 2023, **59**, 1365–1368.
12 Z. Jia, X. Yang, H. Y. Shi, S. Hu and X. Sun, *Chem. Commun.*, 2022, **58**, 5905–5908.
13 L. Xie, W. Xiao, X. Shi, J. Hong, J. Cai, K. Zhang, L. Shao and Z. Sun, *Chem. Commun.*, 2022, **58**, 13807–13810.
14 H. Fei, Y. Lin and M. Wei, *J. Colloid Interface Sci.*, 2014, **425**, 1–4.
15 P. He, J. Liu, X. Zhao, Z. Ding, P. Gao and L.-Z. Fan, *J. Mater. Chem. A*, 2020, **8**, 10370–10376.
16 J. Hu, H. Chen, K. Xiang, L. Xiao, W. Chen, H. Liao and H. Chen, *J. Alloys Compd.*, 2021, **856**, 157085.
17 M. Tamilselvan, T. V. M. Sreekanth, K. Yoo and J. Kim, *Appl. Surf. Sci.*, 2020, **529**, 147077.
18 Z. Wu, J. Yao, C. Chen, X. Chen, X. Pan, J. Zheng, Y. Gan, J. Li, X. Liu, C. Xia, L. Lv, H. Wang and H. Wan, *Chem. Eng. J.*, 2024, **479**, 147889.
19 M. Liao, J. Wang, L. Ye, H. Sun, Y. Wen, C. Wang, X. Sun, B. Wang and H. Peng, *Angew. Chem., Int. Ed.*, 2020, **59**, 2273–2278.
20 W. Wang, D. Liu, Y. Jiang, D. Zhang, X. Shen, S. Li, J. Liang and H. Xu, *Chem. Eng. J.*, 2023, **463**, 142309.
21 Y. Liu and X. Wu, *J. Energy Chem.*, 2023, **87**, 334–341.
22 J. Shin, D. S. Choi, H. J. Lee, Y. Jung and J. W. Choi, *Adv. Energy Mater.*, 2019, **9**, 1900083.
23 L. Shan, J. Zhou, W. Zhang, C. Xia, S. Guo, X. Ma, G. Fang, X. Wu and S. Liang, *Energy Technol.*, 2019, **7**, 1900022.
24 P. Shvets, O. Dikaya, K. Maksimova and A. Goikhman, *J. Raman Spectrosc.*, 2019, **50**, 1226–1244.
25 S. Ni, G. Zhou, S. Lin, X. Wang, Q. Pan, F. Yang and D. He, *Mater. Lett.*, 2009, **63**, 2459–2461.
26 X. Y. Chen, L. B. Wang, H. Li, F. Y. Cheng and J. Chen, *J. Energy Chem.*, 2019, **38**, 20–25.
27 Z. Lishang, H. Jisong, Z. Bao, L. Jia, W. Houzhao, M. Ling and J. Jianjun, *J. Mater. Chem. A*, 2021, **9**, 7631.
28 J. Lai, H. Zhu, X. Zhu, H. Koritala and Y. Wang, *ACS Appl. Energy Mater.*, 2019, **2**, 1988–1996.
29 P. Hu, T. Zhu, X. Wang, X. Wei, M. Yan, J. Li, W. Luo, W. Yang, W. Zhang, L. Zhou, Z. Zhou and L. Mai, *Nano Lett.*, 2018, **18**, 1758–1763.
30 Y. Xu, X. Deng, Q. Li, G. Zhang, F. Xiong, S. Tan, Q. Wei, J. Lu, J. Li, Q. An and L. Mai, *Chemistry*, 2019, **5**, 1194–1209.